Trace element partitioning in sedimentary pyrite controlled by nanoscale processes

Q. Deng, P. Le Pape, F. Poitrasson, C. Duquenoy, R. Guilbaud, A. Somogyi, N. Mehta, F. Guyot, L. Delbes, Ö. Ataytür, R. Messias, E. Bourbon, K. Benzerara, G. Morin

Supplementary Information

The Supplementary Information includes:

1. Synthesis Procedure of Pyrite with Trace Elements

All experiments were performed at room temperature (22°C ± 3 °C). To prevent oxidation of the reduced iron sulphide solids, all syntheses were performed in a Jacomex^{TM} glovebox (< 5 ppm O_2) using degassed Milli-Q water (previously prepared by bubbling with N_2 at 80°C for 45 min).

A brand new pure-grade $FeCl_3 \cdot 6H_2O$ salt (Sigma-Aldrich #44944-SIGALD; CAS 10025-77-1; 0.5 ≤ TE ≤ 50 ppm) was used to prepare an acidic Fe (III) stock solution at 0.625 M in O_2-free milli-Q water. Similarly, a brand-new $Na_2S \cdot 9H_2O$ ≥ 99.99% trace-metal basis (Sigma-Aldrich #MKBT8258V; 0.1-50 ppm) salt was used to prepare the HS^- stock solution at 0.629 M. In addition, a multi-element solution containing multiple trace elements (see Table S-2 for detailed compositions) was poured to fill a glass vial (30 mL), sealed with a butyl stopper and brought into

the glove box and opened to stirred at a low speed on a magnetic stirring plate overnight to equilibrate it under a N_2 atmosphere.

Table S-1 Proportions of reactants used for pyrite synthesis with 1 ppm, 100 ppb trace elements and control group (adapted from Baya *et al.*, 2022).

Sample	Reactants	Stock solutions		Reaction vial	
		C (M)	V (mL)	n (mmol)	c (mM)
Py_1ppm	$FeCl_3 \cdot 6H_2O$	0.625	1	0.625	12.5
	TE solution	0.00081*	1	0.00081	0.0162
	$Na_2S \cdot 9H_2O$	0.629	1	0.629	12.6
	O_2-free mQ water		47		
	Total		50		
Py_100 ppb	$FeCl_3 \cdot 6H_2O$	0.625	1	0.625	12.5
	TE solution	0.000081*	0.1	0.000081	0.00162
	$Na_2S \cdot 9H_2O$	0.629	1	0.629	12.6
	O_2-free mQ water		47.9		
	Total		50		
Py_control	$FeCl_3 \cdot 6H_2O$	0.625	1	0.625	12.5
	$Na_2S \cdot 9H_2O$	0.629	1	0.629	12.6
	O_2-free mQ water		48		
	Total		50		

Note: *Calculated with 50 mg. L^{-1} in the multielement standard solution (Table S-2).

The syntheses were performed in a 100 mL glass vial sealed with a butyl rubber stopper. The synthesis protocol consisted in mixing the Fe(III) solution with an appropriate volume of the TE stock solution and then mixing the Fe/TE solution with the HS^- solution in a 1:1 stoichiometric ratio and ageing the mixture under vigorous stirring for at least a week. Pyrite nucleation generally starts after a few days or months, depending on the trace metals added during the synthesis (Noël *et al.*, 2014, 2015; Morin *et al.*, 2017; Le Pape *et al.*, 2017; Baya *et al.*, 2021, 2022; Deng *et al.*, 2025). Two identical batches were performed for each concentration of TE in the starting solution (control, 100 ppb, 1 ppm): the first batch was stopped after the formation of pyrite (141 h, 216 h, 380 h) when the colour of the solid turned dark grey (freshly formed), and the second batch was stopped approximately 1 month (~1000 h) after the second batch, once having reached a steady state with the remaining aqueous TE. Thus, the latter is referred to as final (aged) pyrite in Table 1. An extra batch, using degassed milli-Q water for synthesis and a magnetic stirrer, was run alongside the

control groups and stopped with the third batch for chemical analysis to assess potential contamination from the materials.

When each batch was stopped, the synthesis suspension was poured into two centrifuge tubes (50 mL) of equal volume. After centrifugation at 6000 rpm for 10 min, the supernatant was carefully poured into another tube (50 mL). It was then filtered (Nylon 0.2 µm) and stored in a tube (15 mL). The solid was then rinsed twice with O_2-free Milli-Q water to avoid NaCl precipitation during drying, then centrifuged at 6000 rpm for 12 min. The rinsed solid was vacuum-dried in a desiccator in the glovebox for one day.

Table S-2 Mass concentration (w/v) ± expanded measurement uncertainty of all elements in the ICP multielement standard solution in 1% HNO_3 Suprapur ® provided by Merck, compared with our ICP-MS data.

Element	Certified value (mg · L^{-1})	Uncertainty (mg · L^{-1})	Measured values by ICP-MS (mg · L^{-1})
Al	49	±5	
As	48	±5	60.8
Ba	47	±5	
Cd	49	±5	
Co	48	±5	43.9
Cr	48	±5	
Cu	47	±5	43.8
K	502	±50	
Mn	49	±5	46.4
Mo	49	±5	
Ni	49	±5	48.6
Se	49	±5	61.9
Sr	50	±5	
Zn	50	±5	43.6

2. Pyrite Synthesis Reaction Sequences

The reaction sequence starts with the reduction of $Fe^{3+}_{(aq)}$ to $Fe^{2+}_{(aq)}$ by half of the supplied H_2S (Morin *et al.*, 2017; Deng *et al.*, 2025). The remaining H_2S reacts with half of the formed Fe^{2+} to produce $FeS_{(s)}$ and elemental $S^{(0)}$, and pyrite is then formed by the reaction between $FeS_{(s)}$ and $S^{(0)}$ (Le Pape *et al.*, 2017; Baya *et al.*, 2022; Deng *et al.*, 2025), *via* the polysulfide pathway (Rickard

and Luther, 2007). When strict equimolar quantities of $Fe^{3+}_{(aq)}$ and H_2S are introduced, 50% of the initial $Fe^{3+}_{(aq)}$ amount, $[Fe]_0$, is converted into pyrite.

Although the starting reactants contains $Fe^{3+}_{(aq)}$ (Morin *et al.*, 2017; Le Pape *et al.*, 2017; Baya *et al.*, 2022; Deng *et al.*, 2025), it is immediately reduced to $Fe^{2+}_{(aq)}$ by half of the supplied H_2S with subsequent formation of $S^{(0)}$, yielding secondary starting conditions that are comparable with other studies using protocols in which Fe^{2+} or FeS are reacted with polysulfides (Rickard and Luther, 2007) or $S^{(0)}$ (Swanner *et al.*, 2019; Lin *et al.*, 2022). The efficiency of our Fe^{3+}-based protocol in producing pure pyrite at ambient temperature relies on the concomitant and early formation of nanosized poorly crystalline mixed-valent FeS precursors together with polysulfides that partially precipitate as $S^{(0)}$ (Morin *et al.*, 2017; Deng *et al.*, 2025; Poitrasson *et al.*, 2026). In comparison, methods based on $S^{(0)}$ addition depend on the ability of this sparingly soluble solid to dissolve into polysulfides, thus generally necessitating heating the suspension to obtain pyrite (Swanner *et al.*, 2019; Lin *et al.*, 2022). When the two initial reactants ($Fe^{3+}_{(aq)}$ and H_2S) are not in strict equimolar proportions, the pyrite synthesis yield is less than 50% of $[Fe]_0$ as discussed in the text.

3. Mineralogical composition of pyrite products

Powder XRD analyses reveal the kinetic influence of multi-trace elements on pyrite formation. Even with the presence of both known nucleation accelerators and inhibitors as shown in previous studies (Morin *et al.*, 2017; Le Pape *et al.*, 2017; Baya *et al.*, 2021, 2022), the combination of TEs has an acceleration effect on the kinetics of pyrite formation. Pyrite was first detected by XRD after approximately 141 h of synthesis, when 1 ppm of the TEs was added to the synthesis medium. The control group has the slowest formation rate, as pyrite was first observed at 380h. The concentration of TEs is positively correlated with the pyrite nucleation rate. However, since the added TE solution is acidic (1 wt% HNO_3), the pH across these three synthesis groups decreases with increasing TE solution quantity, ranging from 3 to 5 (Table S-4).

Table S-3 Unit-cell parameters, crystallite sizes and proportions of mineralogical phases obtained from Rietveld refinement or XRD powder patterns. Uncertainties given in brackets refer to the last digit. Other crystallographic parameters were fixed. Starting crystal structure data were taken from Wyckoff (1963), Buerger (1937) and Lennie *et al.* (1995) for pyrite, marcasite and mackinawite, respectively. Unit-cell parameters of mackinawite were fixed to those reported by Baya *et al.* (2021). The patterns were refined using the XND 1.3 code (Berar and Baldinozzi, 1998). The – sign indicates the same value as the previous one in the same row.

Sample **Mineral phases**	***a*** **(Å)**	***b*** **(Å)**	***c*** **(Å)**	**MCD** $_{iso}$ **(nm)**	**MCD** $_{[111]}$ **(nm)**	**MCD** $_{[001]}$ **(nm)**	**wt %**
Py_1ppm_141hr							
pyrite	5.44(2)	-	-		7(1)	23(2)	63(3)
marcasite	4.4(1)	5.4(1)	3.36(8)	6			25(4)
mackinawite	3.7	3.7	5.2	2			12(2)
Py_1 ppm_1030hr							
Pyrite	5.44(2)	-	-		6(1)	24(3)	61(3)
Marcasite	4.41(8)	5.4(1)	3.39(6)	8(4)			24(5)
mackinawite	3.7	3.7	5.2	2			15(3)
Py_100ppb_216hr							
pyrite	5.44(1)	-	-		6(1)	23(2)	70(2)
marcasite	4.40(9)	5.5(1)	3.37(7)	7(3)			22(5)
mackinawite	3.7	3.7	5.2	2			8(1)
Py_100ppb_1004hr							
pyrite	5.44(1)	-	-		7(1)	24(2)	64(3)
marcasite	4.37(5)	5.46(7)	3.43(4)	15(13)			14(4)
mackinawite	3.7	3.7	5.2	23			22(2)
Py_control_380hr							
pyrite	5.44(1)	-	-		6(1)	21(2)	70(2)
marcasite	4.39(9)	5.5(1)	3.36(7)	6(3)			19(4)
mackinawite	3.7	3.7	5.2	2			11(1)
Py_control_1053hr							
pyrite	5.42(4)	-	-		5(2)	18(4)	70(6)
mackinawite	3.7	3.7	5.2	2			30(5)

Rietveld refinement of XRD powder patterns indicated an average of 84(7) wt% of FeS2, represented by 61-70 wt% pyrite (FeS2) and 0-25 wt% marcasite (FeS2), accompanied by 8-30 wt% of residual poorly crystalline mackinawite (FeS) (Fig. S-1; Table S-3). The presence of marcasite is explained by the slightly acidic pH of 3-6 in our experiments (Table S-4), consistent with previous studies (Schoonen and Barnes, 1991, and references therein). Moreover, we observe a negative correlation between the proportion of marcasite and pH. Since the TE concentration is not the only parameter that varies, it cannot be concluded with certainty that the formation rate only depends on the concentration of TE.

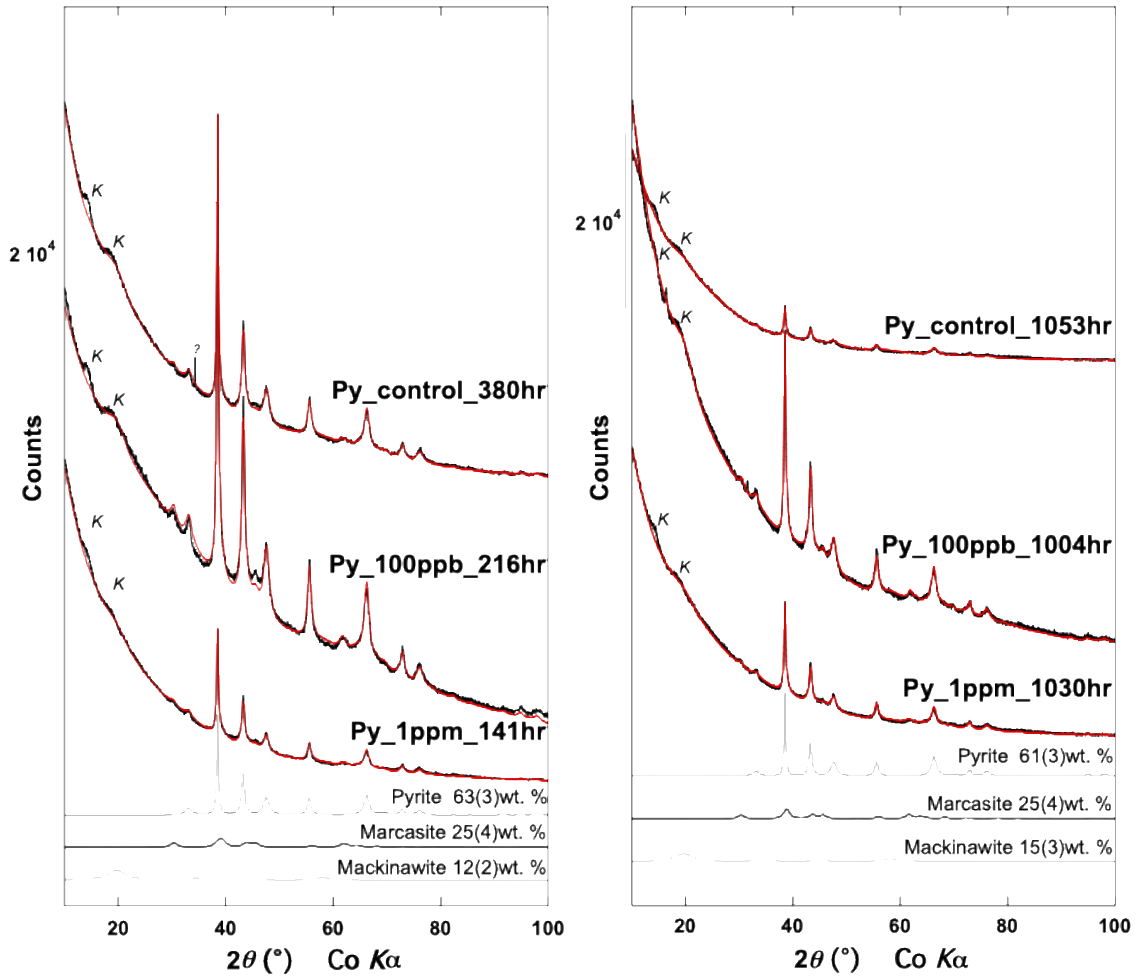

Figure S-1 Rietveld refinement (red) of experimental powder XRD patterns (black) of freshly precipitated pyrites of the three experiments (left) and aged pyrites products of the three experiments (right). The mineralogical composition at the bottom is that of Py_1ppm_141hr (left) and Py_1ppm_1030hr (right).

Table S-4 Measured pH values at the start and end of all syntheses.

Synthesis	pH_{start} (±0.02)	pH_{end} (±0.02)
Py_1 ppm_141hr	4.52	3.12
Py_1 ppm_1030hr	4.49	3.20
Py_100ppb_216hr	4.87	5.11
Py_100ppb_1004hr	4.86	4.50
Py_control_380hr	6.01	5.54
Py_control_1053hr	6.10	4.40

A small amount of remaining nano-mackinawite is also detected for all final pyrite products (Table S-3), which is attributed to the minor presence of untransformed solid precursor. Identified as FeS by Morin *et al.* (2017), the phase is a major component (47 mol%) of the solid precursor in our synthesis method. This was previously demonstrated using XRD-Rietveld, wide-angle X-ray scattering-pair distribution function, and Fe K-edge EXAFS analyses by Baya *et al.* (2021). The actual amount of residual nano-mackinawite is, however, difficult to quantify using the sole XRD-Rietveld analysis since the broad basal reflection of nano-mackinawite at 20° 2θ is difficult to distinguish from the second bump signal of the sample-chamber Kapton window.

4. Chemical analysis of supernatant solutions by ICP-MS

The filtered supernatants of all the synthesis batches were diluted and acidified (HNO_3) for chemical analysis and then stored in a refrigerator until chemical analysis.

In the Jacomex™ glove box (O_2 < 5 ppm), acid (HNO_3) washed and labelled Falcon tubes (15 mL) were weighed on a balance with their own labelled lids. The filtered supernatants of the assigned volumes were added to the corresponding tubes using a suitable micropipette. Each tube was weighed individually using the same balance. Degassed Milli-Q water was added to each tube to meet the calculated dilution factor (see Table S-1 for details). All the tubes were weighed again. The tubes were removed from the glove box via the airlock, and the calculated volume of analytical-grade HNO_3 was added to each tube to achieve a concentration of 0.37 M. The tubes were then stored in a refrigerator until analysis.

Elemental analysis was carried out at the GET laboratory using a triple quad ICP-MS (iCAP-TQ, Thermo Fisher Scientific) in SQ-KED (Simple Quad-Kinetic Energy Discrimination) mode with He as a collision gas for the masses ^{55}Mn, ^{56}Fe, ^{59}Co, ^{60}Ni, ^{63}Cu and ^{66}Zn, and in TQ-O_2 mode with O_2 as a reaction gas for ^{80}Se and ^{75}As. Nitric acid (3%) blanks were analysed regularly to monitor instrument cleanliness and were subtracted from the samples and standards. Instrument external calibration was conducted using elemental standards ranging from 20 ppt to 2 ppb (Co and Cu), 40 ppt to 4 ppb (As), 200 ppt to 20 ppb (Zn, Se) and 2 ppb to 200 ppb (Mn and Ni), taken from a multi-elemental solution (SCP SCIENCE, Canada) and Fe with concentrations ranging from 2 ppb to 2 ppm produced from an Atomic Absorption Spectroscopy standard. Indium doping for internal calibration was done at ~2 ppb. Uncertainties were estimated to be ± 5% RSD for most elements (Zn was an exception with deviations between 11 to 14% relative to the expected values) on the basis of the analysis of the EPOND (multi-elemental solution EPOND SA, Switzerland) and

SLRS-6 (Canadian riverine certified reference waters). In addition, and given the large dynamic range between TE and Fe implied by the concentrations of the studied samples, ICP-MS Fe concentration determinations were checked by Atomic Absorption Spectroscopy using a AAnalyst 400 (Perkin Elmer) instrument fitted with a hollow cathode lead lamp (λ = 248.33nm). Instrument calibration was performed on a 0 to 5 ppm Fe concentration range, and the measurement of a reference solution was acceptable within <1% of the accepted value. Uncertainties were estimated to be ± 2% RSD, based on the long-term reproducibility of a standard solution. The two analytical techniques yielded Fe concentrations that agreed to within 10%. Iron concentration results are reported in Table S-5.

Table S-5 ICP-MS analysis of initial ($[Fe]_0$) and final aqueous Fe concentration ($[Fe^{2+}]_{(aq)}$) in the synthesis supernatants, and corresponding calculated values of x_{py}/y of each reaction.

Synthesis	x_{py}/y	$[Fe]_0$	$[Fe^{2+}]_{(aq)}$
		ppm	ppm
Py_1ppm_141hr	0.497	701	353
Py_1ppm_1030hr	0.502	701	349
Py_100ppb_216hr	0.540	701	322
Py_100ppb_1004hr	0.543	701	321
Py_control_380hr	0.504	701	348
Py_control_1053hr	0.549	701	317

The measurement of Fe^{2+}(aq) in the supernatant at the end of the synthesis is required to determine x_{py} or y. The x_{py}/y value for our syntheses ranges from 0.50 to 0.54 (mean 0.52), indicating that the reactants are nearly equimolar, with a slight excess of H_2S in some cases. This can also be confirmed by the presence of FeS after pyrite is formed, as shown in Table S-3.

There is a slight excess of H_2S over Fe^{3+} at the start of the experiments with a $x_{py} > 0.5$. The reaction can be written as:

$$Fe^{3+}_{(aq)} + (½ + y)\ H_2S \rightarrow (y - ½)\ FeS + (1 - y)\ Fe^{2+}_{(aq)} + ½\ FeS_2 + (1+2y)\ H^+ \quad \textbf{(S-1)}$$

in which $0.5 \leq y < 1$ represents the excess of H_2S. This stoichiometry then leads to a residual FeS component at the end of the synthesis, which is detected by XRD (Fig. S-1, Table S-3).

Table S-6 **(a)** ICP-MS and AAS measurements of initial (Fe_0 & TE_0), aqueous (Fe_{aq} & TE_{aq}) and calculated Fe and TE in solid phase (Fe_{solid} & TE_{solid}) in ppb and mol, **(b)** Concentration factors and **(c)** D_{py} for each TE of all samples.

Table S-6 (.xlsx) is available for download from the online version of this article at https://doi.org/10.7185/geochemlet.2622.

Mass balance calculation was performed using Fe and TE concentrations, i.e. $[Fe]_{aq}$ and $[TE]_{aq}$, which were measured by AAS and ICP-MS, respectively (Table S-6). Concentrations of TE in the solid phase were derived by difference between initial and aqueous values, i.e. $[TE]_s = [TE]_0 - [TE]_{aq} / ([Fe]_0 - [Fe]_{aq})$, assuming a FeS_2 stoichiometry for the solid phase. The $[TE]_s/[Fe]_s$ molar ratios could also be estimated from nano-XRF analyses only for these two most concentrated samples (Table S-7; Fig. 1c,d), as detailed thereafter.

5. Nano-X-ray fluorescence data collection and analysis

Two samples of synthetic pyrites were analysed at the Nanoscopium Beamline (SOLEIL synchrotron): Py_1ppm_141hr and Py_1ppm_1030hr.

Nano-XRF hyperspectral maps were measured simultaneously using two Si-drift detectors with a 50 mm^2 useful area (KETEK H50, KETEK GmbH) and XMAP (XIA LLC) fast multichannel analyser cards, and placed at a 20° angle symmetrical to the sample surface (Somogyi *et al.*, 2015).

For Py_1ppm_141hr, fine pyrite powder was deposited on a 5 x 5 mm Si wafer in a Jacomex™ glove box (O_2 < 5 ppm) and then analysed in air at 17.5 keV. Aggregates of pyrite particles were analysed by nano-XRF over a 15 µm x 15 µm area, with a probe size of 150 nm and an integration time of 300 ms per pixel. As such, elemental distribution maps were obtained with a total of approximately 10,500 points.

For Py_1ppm_1030hr, pyrite particles were deposited on a 0.5 x 0.5 mm and 80 µm thick silicon nitride window in a Si wafer in a Jacomex glovebox and then analysed in air at 20.5 keV. Aggregates of pyrite particles were analysed using nano-XRF over a 33 µm x 29 µm area with a probe size of 150 nm and an integration time of 250 ms per pixel. Nano-XRF hyperspectral maps were obtained with a total of approximately 40,000 points.-The elemental maps were corrected for the measured dead time, which ranged from 15 to 50%.

Data processing was performed by using both the MATLAB and the PyMCA softwares. Elemental XRF maps were obtained by selecting photons in specific channels of the detector with a MATLAB package developed at the beamline on the basis of total fluorescence spectra (2 maps for each sample corresponding to each detector). To do so, the total fluorescence spectra (Figs. S-2, S-3) were first fitted using PyMCA by considering both the Fe escape peak as well as pile up peaks. Photons in the channels were carefully selected by minimizing the channels where important convolutions between X-ray emission lines were observed. Using MATLAB, pyrite particle aggregates were detoured by subtracting a background corresponding to all values smaller than a specific threshold defined for each previously selected channel (corresponding to counts coming from one or more X-ray emission lines of particular elements). New elemental maps were obtained and used to examine elemental correlations by plotting vectorised matrices against each other (*e.g.,* Fe Kα against Se Kα). For the plots where applicable, linear regression trend lines were fitted to the data to facilitate interpretation. In addition, TE:Fe ratio was obtained from the ratio of the emission line integrated intensities determined by fitting the spectrum of the whole nano-XRF maps (Figs. S-2 and S-3). In this procedure, the integrated intensity of each emission line considered was normalised using the fluorescence yield values tabulated in Krause (1979). Expected uncertainties on the TE:Fe ratios, due to X-ray reabsorption, are estimated to be less than 5%. Indeed, in this ultra-thin sample configuration, X-ray absorption of the *K*-emission lines through 1 µm thick pure pyrite with its maximum density of 5 g/cm^3 are 6% for Fe at 6.4 keV, 11% for Ni at 7.5 keV, 9% for Cu at 8.0 keV, 8% for Zn at 8.6 keV and 5% for As at 10.5 keV.

Table S-7 Comparison between TE:Fe molar ratio values obtained by ICP-MS measurements (Table S-6) and those obtained from nano-XRF data, using the integrated intensities of the indicated emission lines normalised by corresponding fluorescence yields. The integrated intensities were determined by fitting the whole XRF spectrum of the nano-XRF maps (Figs. S-2 and S-3).

	Py_1ppm_141hr(2)		**Py_1ppm_ 1030hr(3)**		
Ratios (x 10^{-3})	**ICP-MS**	**XRF**	**ICP-MS**	**XRF**	**Emission lines**
Se/Fe	3.19	5.55	2.87	4.41	Fe K_α vs. Se K_α
Ni/Fe	3.28	5.90	2.93	3.82	Fe K_α vs. Ni K_α
As/Fe	3.18	2.27	2.82	5.77	Fe K_α vs. As K_α
Cu/Fe	3.20	3.68	2.87	3.86	Fe K_α vs. Cu K_α
Zn/Fe	6.62	3.82	5.14	2.54	Fe K_α vs. Zn K_α

Note: (2) and (3) indicates measurements with detector #2 or #3, respectively

6. Scanning transmission electron microscopy (STEM)

Scanning transmission electron microscopy (STEM) was performed on TE-doped pyrite samples on carbon-coated Cu grids used as sample holders, using a JEOL 2100F field-emission gun microscope operating at 200 kV. Elemental compositions and qualitative chemical mapping were acquired by energy dispersive X-ray spectroscopy (EDXS) with a Si(Li) JEOL detector to examine the distribution of TE in pyrite solids.

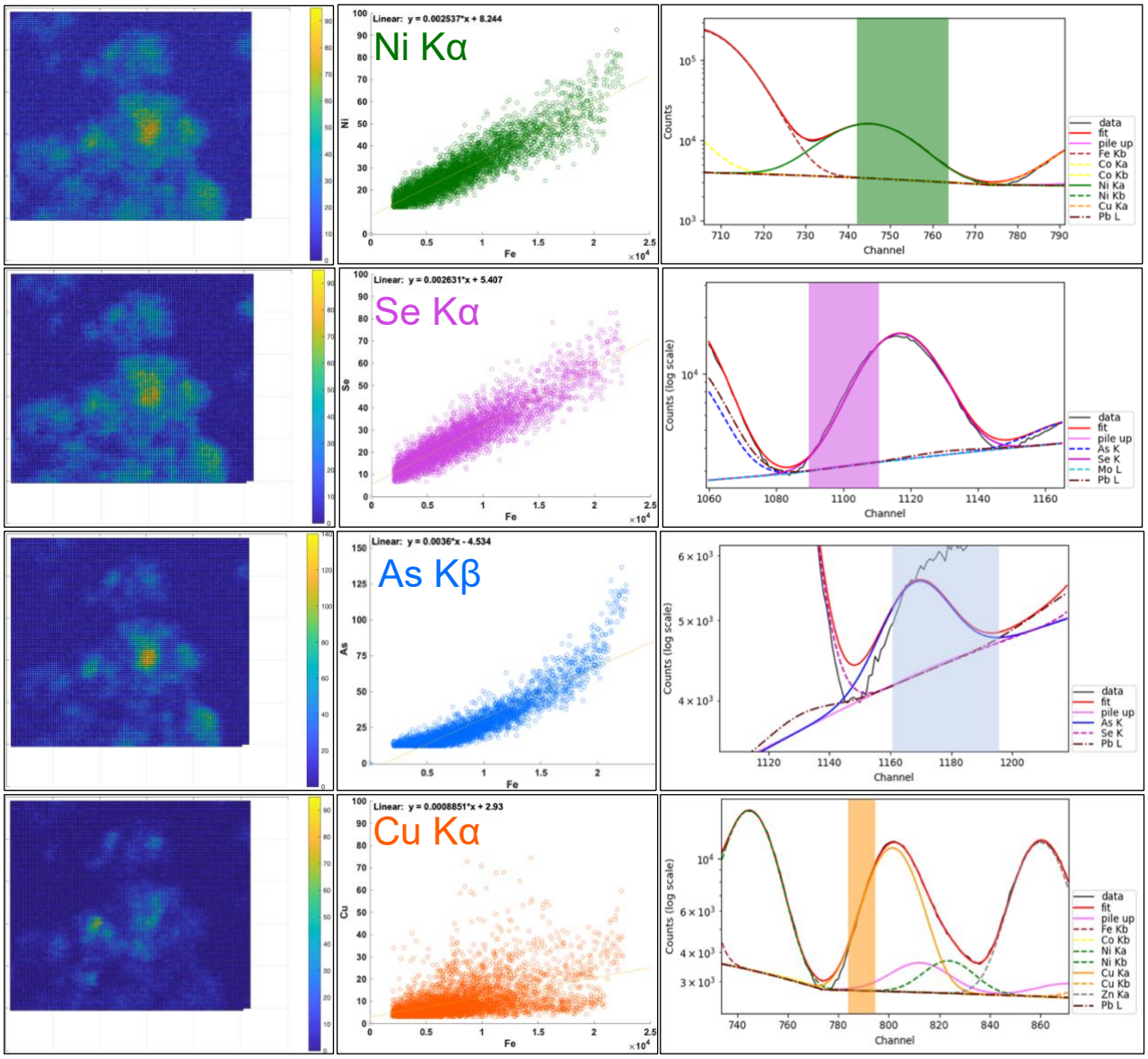

Figure S-2 Nano-XRF elemental map and TE/Fe plots for every pixel on a 15 x 15 µm area for the final sample Py_1ppm_141hr (left panel). Linear regressions, corresponding equations, and correlation coefficients are displayed (middle panel). The selected channel range for each emission line is shown (right panel). The total fitted fluorescence spectrum (bottom left), the STEM-EDX image, and the total spectrum (bottom right) are presented. Figure continued on next page.

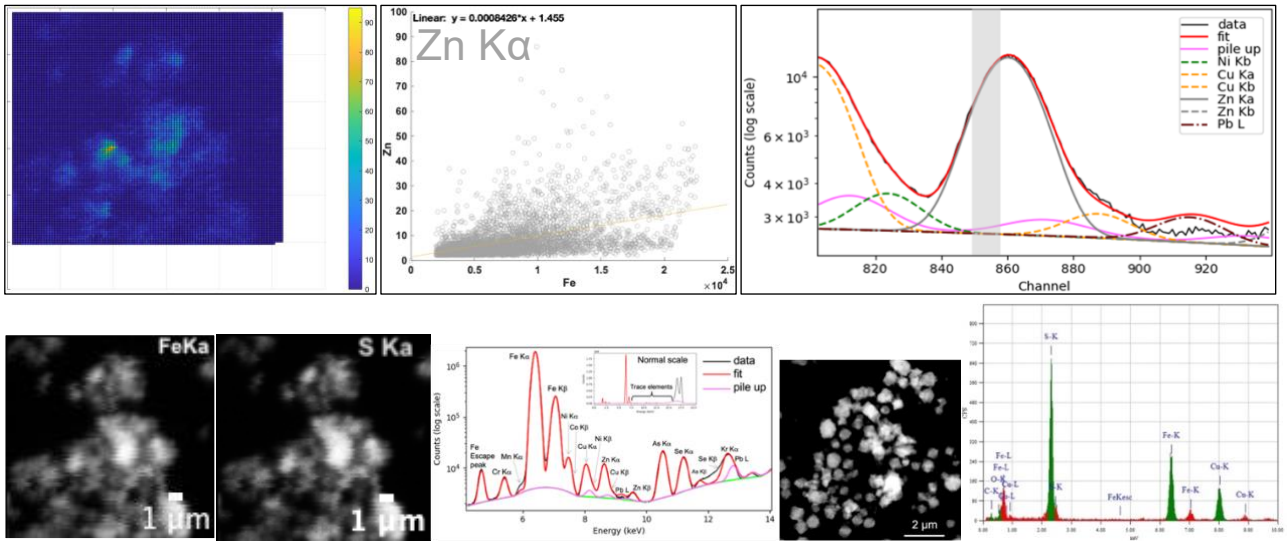

Figure S-2 continued.

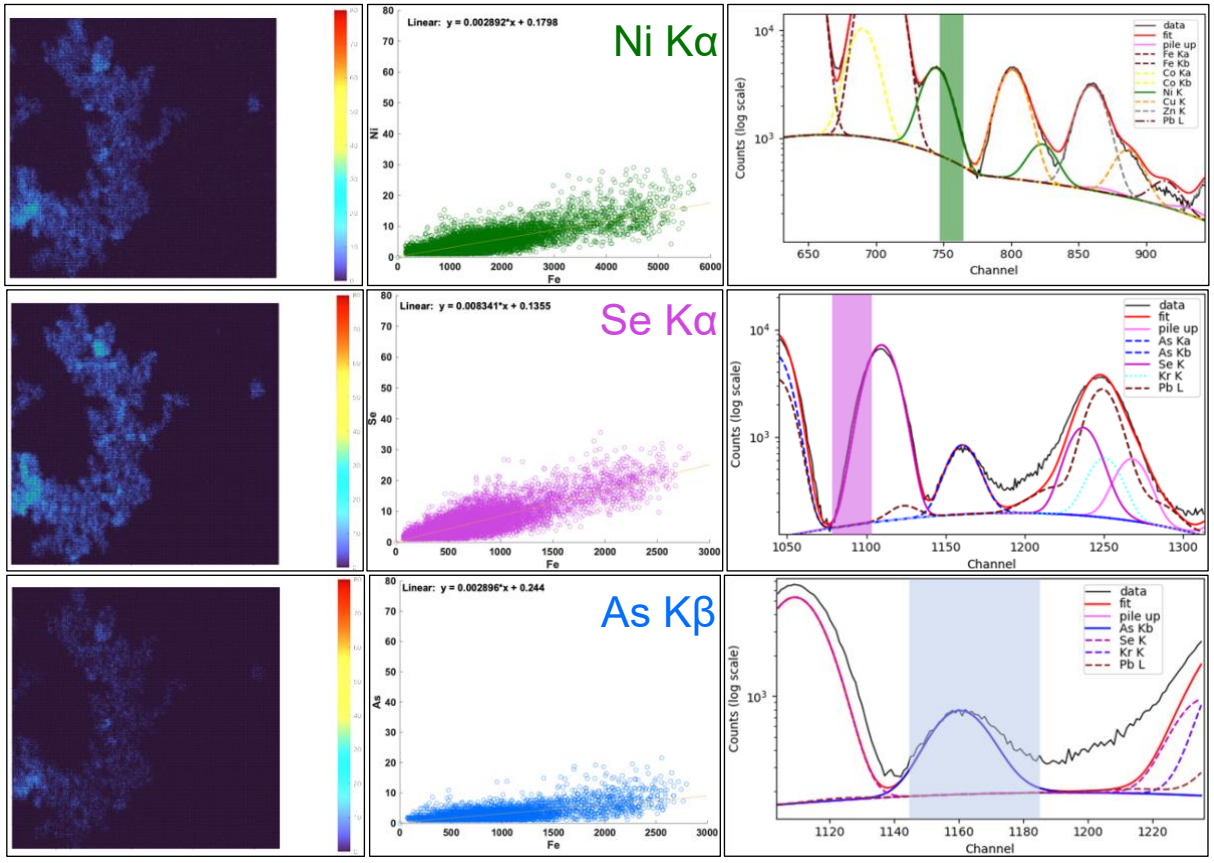

Figure S-3 Nano-XRF elemental map and TE/Fe plots for every pixel on a 33 x 29 µm area for the final sample Py_1ppm_1030hr (left panel). Linear regressions, corresponding equations, and correlation coefficients are displayed (middle panel). The selected channel range for each emission line is shown (right panel). The total fitted fluorescence spectrum (bottom left), the STEM-EDX image, and the total spectrum (bottom right) are presented. Figure continued on next page.

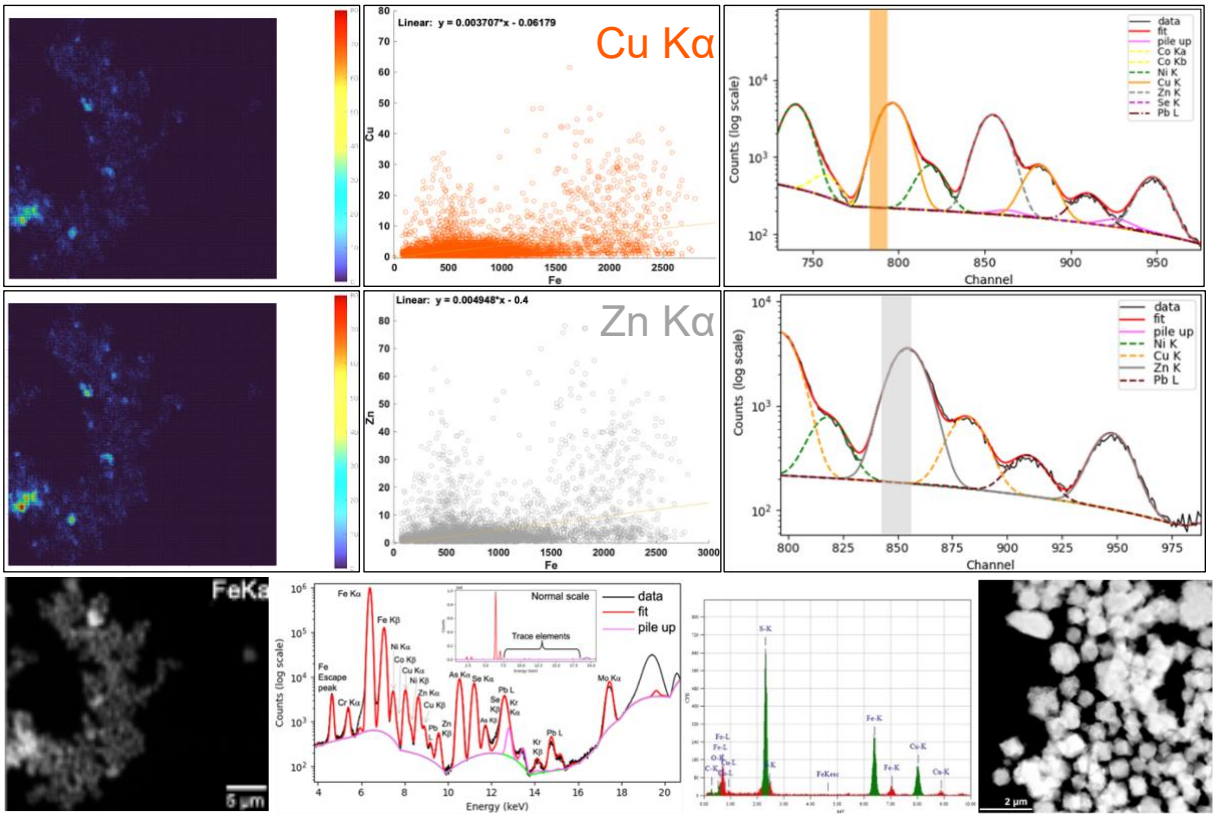

Figure S-3 continued.

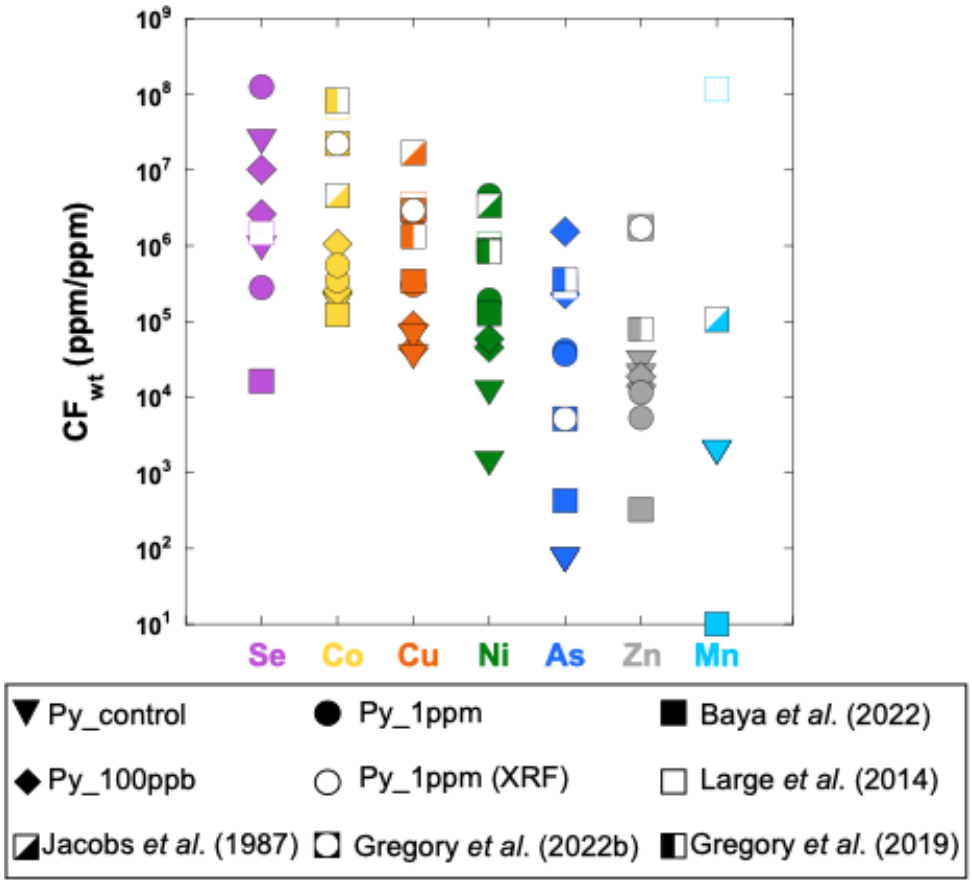

Figure S-4 Concentration factor CF is defined as the ratio of solid to aqueous TE weight concentrations, without applying the 10-4 factor of Large *et al.* (2014). New data points are calculated by the mean TE content in Cariaco pyrite reported by Gregory *et al.* (2022b), median TE content in a set of sedimentary pyrites reported by Gregory *et al.* (2019) and mean TE concentration in the modern ocean (Large *et al.*, 2014).

7. Additional literature insights on the Se-pyrite solid-solution

The Se^{-1} ion generally replaces the S^{-1} ion in the pyrite structure of both synthetic (Diener *et al.*, 2012; Guida *et al.*, 2024) and natural (Matamoros-Veloza *et al.*, 2014; Manceau *et al.*, 2020) samples. Although Se^{-1} is not expected to cluster in the FeS_2-$FeSe_2$ solid solution up to 3 mol% $FeSe_2$ (i.e. 4 wt% Se) (Manceau *et al.*, 2020), inhomogeneous Se distribution has been reported in synthetic pyrites doped at 1.7 wt% Se (Diener and Neumann, 2011), suggesting that the solid-solution can exhibit non-ideality at such a substitution rate, as well as in natural pyrites (Matamoros-Veloza *et al.*, 2014).

Note, according to the Se for S substitution in pyrite, the *D* value for Se should be rigorously calculated with S as the carrier element in Figure 1c. It would result in smaller absolute

D values, but likely with similar trend since the $[S]_{(aq)}$ value is not expected to vary much among our experiments, S being a major constituent.

Supplementary Information References

Baya, C., Le Pape, P., Baptiste, B., Brest, J., Landrot, G., Elkaim, E., Noël, V., Blanchard, M., Ona-Nguema, G., Juillot, F., Morin, G. (2021) Influence of trace level As or Ni on pyrite formation kinetics at low temperature. *Geochimica et Cosmochimica Acta* 300, 333–353. https://doi.org/10.1016/j.gca.2021.01.042

Baya, C., Le Pape, P., Baptiste, B., Menguy, N., Delbes, L., Morand, M., Rouelle, M., Aubry, E., Ona-Nguema, G., Noël, V., Juillot, F., Morin, G. (2022) A methodological framework to study the behavior and kinetic influence of V, Mn, Co, Ni, Cu, Zn, As, Se and Mo during pyrite formation *via* the polysulfide pathway at ambient temperature. *Chemical Geology* 613, 121139. https://doi.org/10.1016/j.chemgeo.2022.121139

Berar, J.F., Baldinozzi, G. (1998) Xnd code: from X-ray laboratory data to incommensurately modulated phases. Rietveld modelling of complex materials. *Commission for Powder Diffraction Newsletter* 20, 3–5.

Buerger, M.J. (1937) Interatomic Distances in Marcasite and Notes on the Bonding in Crystals of Löllingite, Arsenopyrite, and Marcasite Types. *Zeitschrift für Kristallographie - Crystalline Materials* 97, 504–513. https://doi.org/10.1524/zkri.1937.97.1.504

Deng, Q., Le Pape, P., Aufort, J., Blanchard, M., Baptiste, B., Delbes, L., Baya, C., Juillot, F., Ona-Nguema, G., Menguy, N., Guigner, J.-M., Proux, O., Duquenoy, C., Guilbaud, R., Poitrasson, F., Morin, G. (2025) HERFD-XAS evidence for an octahedrally coordinated CoSn-polysulfide precursor as a probe for the mechanism of pyrite formation. *Geochimica et Cosmochimica Acta* 401, 104–121. https://doi.org/10.1016/j.gca.2025.06.003

Diener, A., Neumann, T. (2011) Synthesis and incorporation of selenide in pyrite and mackinawite. *Radiochimica Acta* 99, 791–798. https://doi.org/10.1524/ract.2011.1883

Diener, A., Neumann, T., Kramar, U., Schild, D. (2012) Structure of selenium incorporated in pyrite and mackinawite as determined by XAFS analyses. *Journal of Contaminant Hydrology* 133, 30–39. https://doi.org/10.1016/j.jconhyd.2012.03.003

Gregory, D.D., Cracknell, M.J., Large, R.R., McGoldrick, P., Kuhn, S., Maslennikov, V.V., Baker, M.J., Fox, N., Belousov, I., Figueroa, M.C., Steadman, J.A., Fabris, A.J., Lyons, T.W. (2019) Distinguishing Ore Deposit Type and Barren Sedimentary Pyrite Using Laser Ablation-Inductively Coupled Plasma-Mass Spectrometry Trace Element Data and Statistical Analysis of Large Data Sets. *Economic Geology* 114, 771–786. https://doi.org/10.5382/econgeo.4654

Gregory, D.D., Lyons, T.W., Large, R.R., Stepanov, A.S. (2022b) Ground-truthing the pyrite trace element proxy in modern euxinic settings. *American Mineralogist* 107, 848–859. https://doi.org/10.2138/am-2022-8024

Guida, C., Ramothe, V., Chappaz, A., Simonnin, P., Rosso, K.M., Ding, R.-R., Prieur, D., Scheinost, A.C., Charlet, L. (2024) Revisiting Selenium Interactions with Pyrite: From Adsorption to Coprecipitation. *ACS Earth and Space Chemistry* 8, 67–78. https://doi.org/10.1021/acsearthspacechem.3c00219

Jacobs, L., Emerson, S., Huested, S.S. (1987) Trace metal geochemistry in the Cariaco Trench. *Deep Sea Research Part A. Oceanographic Research Papers* 34, 965–981. https://doi.org/10.1016/0198-0149(87)90048-3

Krause, M.O. (1979) Atomic radiative and radiationless yields for *K* and *L* shells. *Journal of Physical and Chemical Reference Data* 8, 307–327. https://doi.org/10.1063/1.555594

Large, R.R., Halpin, J.A., Danyushevsky, L.V., Maslennikov, V.V., Bull, S.W., Long, J.A., Gregory, D.D., Lounejeva, E., Lyons, T.W., Sack, P.J., McGoldrick, P.J., Calver, C.R. (2014)

Trace element content of sedimentary pyrite as a new proxy for deep-time ocean–atmosphere evolution. *Earth and Planetary Science Letters* 389, 209–220. https://doi.org/10.1016/j.epsl.2013.12.020

Lennie, A.R., Redfern, S.A.T., Schofield, P.F., Vaughan, D.J. (1995) Synthesis and Rietveld crystal structure refinement of mackinawite, tetragonal FeS. *Mineralogical Magazine* 59, 677–683. https://doi.org/10.1180/minmag.1995.059.397.10

Le Pape, P., Blanchard, M., Brest, J., Boulliard, J.-C., Ikogou, M., Stetten, L., Wang, S., Landrot, G., Morin, G. (2017) Arsenic Incorporation in Pyrite at Ambient Temperature at Both Tetrahedral S^{-I} and Octahedral Fe^{II} Sites: Evidence from EXAFS–DFT Analysis. *Environmental Science & Technology* 51, 150–158. https://doi.org/10.1021/acs.est.6b03502

Lin, X., Xia, Y., Wei, G., Zhou, J., Liang, X., Xian, H., Zhu, J., He, H. (2022) Distinct effects of transition metal (cobalt, manganese and nickel) ion substitutions on the abiotic oxidation of pyrite: In view of hydroxyl radical production. *Geochimica et Cosmochimica Acta* 321, 170–183. https://doi.org/10.1016/j.gca.2022.01.026

Manceau, A., Merkulova, M., Mathon, O., Glatzel, P., Murdzek, M., Batanova, V., Simionovici, A., Steinmann, S.N., Paktunc, D. (2020) The Mode of Incorporation of As(-I) and Se(-I) in Natural Pyrite Revisited. *ACS Earth and Space Chemistry* 4, 379–390. https://doi.org/10.1021/acsearthspacechem.9b00301

Matamoros-Veloza, A., Peacock, C.L., Benning, L.G. (2014) Selenium Speciation in Framboidal and Euhedral Pyrites in Shales. *Environmental Science & Technology* 48, 8972–8979. https://doi.org/10.1021/es405686q

Morin, G., Noël, V., Menguy, N., Brest, J., Baptiste, B., Tharaud, M., Ona-Nguema, G., Ikogou, M., Viollier, E., Juillot, F. (2017) Nickel accelerates pyrite nucleation at ambient temperature. *Geochemical Perspectives Letters* 5, 6–11. https://doi.org/10.7185/geochemlet.1738

Noël, V., Marchand, C., Juillot, F., Ona-Nguema, G., Viollier, E., Marakovic, G., Olivi, L., Delbes, L., Gelebart, F., Morin, G. (2014) EXAFS analysis of iron cycling in mangrove sediments downstream a lateritized ultramafic watershed (Vavouto Bay, New Caledonia). *Geochimica et Cosmochimica Acta* 136, 211–228. http://dx.doi.org/10.1016/j.gca.2014.03.019

Noël, V., Morin, G., Juillot, F., Marchand, C., Brest, J., Bargar, J.R., Munoz, M., Marakovic, G., Ardo, S., Brown Jr, G.E. (2015) Ni cycling in mangrove sediments from New Caledonia. *Geochimica et Cosmochimica Acta* 169, 82–98. https://doi.org/10.1016/j.gca.2015.07.024

Poitrasson, F., Le Pape, P., Morin, G., Guilbaud, R., Baya, C., Deng, Q., Rabone, J., Aufort, J., Blanchard, M. (2026) Insights into the acquisition of kinetic iron isotope signatures of pyrite precipitated through the polysulfide pathway. *Earth and Planetary Science Letters* 674, 119729. https://doi.org/10.1016/j.epsl.2025.119729

Rickard, D., Luther, G.W. (2007) Chemistry of Iron Sulfides. *Chemical Reviews* 107, 514–562. https://doi.org/10.1021/cr0503658

Schoonen, M.A.A., Barnes, H.L. (1991) Reactions forming pyrite and marcasite from solution: II. Via FeS precursors below 100°C. *Geochimica et Cosmochimica Acta* 55, 1505–1514. https://doi.org/10.1016/0016-7037(91)90123-M

Somogyi, A., Medjoubi, K., Baranton, G., Le Roux, V., Ribbens, M., Polack, F., Philippot, P., Samama, J.-P. (2015) Optical design and multi-length-scale scanning spectro-microscopy possibilities at the Nanoscopium beamline of Synchrotron Soleil. *Journal of Synchrotron Radiation* 22, 1118–1129. https://doi.org/10.1107/S1600577515009364

Swanner, E.D., Webb, S.M., Kappler, A. (2019) Fate of cobalt and nickel in mackinawite during diagenetic pyrite formation. *American Mineralogist* 104, 917–928. https://doi.org/10.2138/am-2019-6834

Wyckoff, R.W.G. (1963) *Crystal Structures, Volume 1*. Interscience Publishers, New York.